Multithermal Jet Formation Triggered by Flux Emergence

Xiaohong Li[ID], Rony Keppens[ID], and Yuhao Zhou[ID]
Centre for mathematical Plasma Astrophysics, Department of Mathematics, KU Leuven, Celestijnenlaan 200B, B-3001, Leuven, Belgium; xiaohong.li@kuleuven.be

Abstract

Flux emergence is responsible for various solar eruptions. Combining observation and simulations, we investigate the influence of flux emergence at one footpoint of an arcade on coronal rain as well as induced eruptions. The emergence changes the pressure in the loops, and the internal coronal rain all moves to the other side. The emerging flux reconnects with the overlying magnetic field, forming a current sheet and magnetic islands. The plasma is ejected outwards and heated, forming a cool jet ∼6000 K and a hot X-ray jet ∼4 million Kelvin (MK) simultaneously. The jet dynamical properties agree very well between observation and simulation. In the simulation, the jet also displays transverse oscillations with a period of 8 minutes, in a so-called whiplike motion. The movement of the jet and dense plasmoids changes the configuration of the local magnetic field, facilitating the occurrence of the Kelvin–Helmholtz instability, and vortex-like structures form at the boundary of the jet. Our simulation clearly demonstrates the effect of emergence on coronal rain, the dynamical details of reconnecting plasmoid chains, the formation of multithermal jets, and the cycling of cool mass between the chromosphere and the corona.

Supporting material: animations

1. Introduction

Magnetic flux emergence has been accepted to be essential for many solar activities. For example, the emergence of flux tubes from the convection zone into the solar atmosphere triggers the formation of sunspots and solar active regions (ARs) (Zwaan 1985, 1987; Cheung et al. 2010; van Driel-Gesztelyi & Green 2015; Chen et al. 2017). Also, the interaction between the preexisting field and the emerging flux could lead to various eruptions, through magnetic reconnection or instabilities (Heyvaerts et al. 1977; Feynman & Martin 1995; Chen & Shibata 2000; Kliem & Török 2006; Chen 2011; Cheung & Isobe 2014; Jiang et al. 2016; Toriumi & Wang 2019). Unprecedented high-resolution observations have provided us with unique opportunities to investigate flux emergence and its associated dynamics in different solar atmospheric layers, such as the triggering of spicules, Hα surges, extreme ultraviolet (EUV) or X-ray jets, and flares (Schrijver 2009; Guglielmino et al. 2010; Schmieder et al. 2014; Guglielmino et al. 2018; Wang et al. 2020; Shen et al. 2022).

As it is hard to study all facets of magnetic flux emergence through observations, numerical magnetohydrodynamic (MHD) simulations have been employed to mimic the emergence of nontwisted or twisted flux tubes into the solar atmosphere and their corresponding eruptions (Shibata et al. 1989; Caligari et al. 1995; Fan 2001; Archontis et al. 2004; Manchester et al. 2004; Cheung & Isobe 2014; Fan 2021). Yokoyama & Shibata (1995, 1996) showed that reconnection between the emerging flux and the overlying magnetic field could drive a microflare, an Hα surge, and an EUV jet

simultaneously. Moreno-Insertis et al. (2008) compared the result of a three-dimensional (3D) MHD simulation with Hinode observations and found that various properties of the jet, such as timescales and velocities, are in agreement with observations. Leake et al. (2013, 2014) found that, without the reconnection between the emerging field with the preexisting field, there would not be eruptions, and the system will develop into a quasistatic equilibrium. Clearly, magnetic reconnection is not only a consequence of the flux emergence but also the driver of the later eruptions. Many flux emergence simulations ignore the turbulent convection in the solar interior and treat the subsurface layers as adiabatically stratified or through externally provided boundary conditions. These idealized simulations have sometimes limited treatment of the energy transfer mechanisms such as thermal conduction, radiative losses, or background heating but allow focus on the essential physical processes in the higher solar atmosphere (Shimojo et al. 2001; Miyagoshi & Yokoyama 2004; Lionello et al. 2016; Török et al. 2016). Realistic simulations with a convective zone layer, which include advanced radiation transfer aspects, are a more self-consistent approach to study flux emergence, which help us understand how convective motion can affect the origin and evolution of the coronal magnetic fields (Nóbrega-Siverio et al. 2016; Moreno-Insertis et al. 2018; Cheung et al. 2019; Hansteen et al. 2019; Nóbrega-Siverio & Moreno-Insertis 2022; Toriumi 2022). Despite these advancements, realistic simulations are challenging and hard to independently reproduce and validate as the combined plasma and radiative physics from the solar interior to the upper layers are complex. Idealized simulations can isolate and study specific mechanisms that may be obscured in more complex realistic simulations. Here, we include all the necessary physical mechanisms without going to full subphotosphere-to-corona evolutions.

In this Letter, we report a solar eruption event triggered by magnetic flux emergence, where some fascinating multithermal

aspects can be witnessed: the effect of jets on coronal rain, the guiding of both hot and cold matter along a neighboring coronal loop system, and intricate up- and down-cycling of cool matter flows. We then present a 2.5D MHD simulation on coronal rain with emerging flux on one side of the coronal loops to study the influence of the emerging flux on the chromospheric and coronal plasma. The simulation is idealized but fully reproducible and includes all the important physical mechanisms, such as optically thin radiative cooling, field-aligned thermal conduction, gravity, and background heating. Contrary to "self-consistent" models, our heating is parametrically inserted and not due to hyperdiffusive visco-resistive effects. Our simulation is in good agreement with the observation: we see how changes in the magnetic field guide the motion of the plasma but also how the motion of the plasma affects the configuration of the magnetic field. This Letter is organized as follows. First, we describe the details of the observations in Section 2; then we present the numerical setup of our simulations in Section 3. Section 4 lists the results of our simulations, and the conclusions and discussion are given in Section 5.

2. Observation

An EUV jet was observed at the solar limb on 2014 October 9 by the Solar Dynamics Observatory (SDO; Pesnell et al. 2012) and the Interface Region Imaging Spectrograph (IRIS; De Pontieu et al. 2014) satellites. We present the Atmospheric Imaging Assembly (AIA; Lemen et al. 2012) 304 Å images from SDO and IRIS 1400 Å slit-jaw images (SJIs) of this event in Figure 1 (and the associated online animation). 1400 Å SJIs have a pixel size of $0''166$ and a cadence of 19 s, while the spatial sampling of the 304 Å images is $0''6$ pixel^{-1} and the cadence is 12 s. We also use data from the spectrograph on IRIS in 1402.77 Å to measure the Doppler shift. As shown in the accompanying animation, there is a coronal loop system at the west limb of the solar surface, with coronal rain material inside it (see Figure 1, panels (a1) and (b1)). At around 19:10 UT, chromospheric matter is ejected upwards at the northern footpoints of the loops and then develops into an EUV jet, denoted by the green arrows in the AIA 304 Å movie (see the online animation and Figure 1(a2)). From the movie, we can also see that a small bright loop emerges from the north side of the coronal loop (see the green arrow in Figure 1(a1)). Following the emergence, the jet becomes bigger and brighter, as shown in Figure 1(a2). As the emerging flux moves upwards, plasmoid structures form at the top of the interaction zone with the preexisting field (indicated in Figure 1(a3)), and these are ejected outwards, becoming part of the jet. This jet flows along the loop system, which is 80 Mm long and 40 Mm high. IRIS only captures the development of the jet, with its smaller field of view as shown by the green rectangle in panel (a1). At 19:34 UT, the jet was moving upwards, as shown in panel (b2). Analyzing a slice along the position denoted by the dashed line "A–B" (panel (b2)), we find that the upward velocity of the jet is about 39 km s^{-1} (the time–distance view is provided in panel (d)). Panel (c) displays the appearance of the Si IV 1403 Å spectra in the slit range of panel (b2) for Doppler velocities from −150 to 150 km s^{-1} when the jet is moving upwards. The green curve is the observed profile along the dashed line, and the red curve is the corresponding single-Gaussian fitting. We can see that the jet has a clear Doppler blueshift with a velocity of 80 km s^{-1}. At the late stage of the

jet, that is, after around 20:00 UT, there are backflows with velocities of about 25 km s^{-1}, and cool matter drops back to the northern footpoints of the loops (see panel (d)). This observation shows how a preexisting multithermal loop system, containing coronal rain, gets affected by flux emergence and reshuffles both cool and hot material along an extended neighboring loop system. We use MHD simulations to better understand these complex plasma processes involving eruption, reconnection, and chromospheric matter recycling.

3. Numerical Setup

Using the parallelized Adaptive Mesh Refinement Versatile Advection Code (MPI-AMRVAC[1]; Keppens et al. 2012; Porth et al. 2014; Xia et al. 2018; Keppens et al. 2021), we perform a 2.5D simulation following the setup in our previous work where we studied realistic coronal rain cycles in a randomly heated arcade system (Li et al. 2022). To be consistent with the observations as discussed in Section 2, we change our domain to a Cartesian (x, y) box with x-axis from -60 to 60 Mm and y-axis from 0 to 60 Mm, and the effective resolution is 39 km in both directions. The system is relaxed to a quasi-equilibrium state using an exponentially decaying background heating, and then a randomized heating pattern is added to mimic the energy input from the lower solar atmosphere, as adopted in Zhou et al. (2020) and Li et al. (2022). After about 143.1 minutes of localized heating, there are condensations in the loops, corresponding to the observed coronal rain inside the loops. Then we add an emerging flux region near the left footpoints of the loops to determine its influence on the raining loops.

For the realization of an emerging magnetic flux, we prescribe a time-dependent electrical field at the lower boundary (Fan & Gibson 2004). This electric field corresponds to a magnetic dipole $\boldsymbol{B}_1$ moving upwards at a constant speed $\boldsymbol{v}$:

$$\boldsymbol{E} = -\boldsymbol{v} \times \boldsymbol{B}_1. \tag{1}$$

where $\boldsymbol{v} = v_0 \, \hat{\boldsymbol{y}}$, and

$$B_{1x} = -B_1 \cos\left(\frac{\pi(x-x_0)}{L}\right) \sin\theta_1 \exp\left(-\frac{\pi \sin\theta_1(y-y_0(t))}{L}\right),$$

$$B_{1y} = B_1 \sin\left(\frac{\pi(x-x_0)}{L}\right) \exp\left(-\frac{\pi \sin\theta_1(y-y_0(t))}{L}\right),$$

$$B_{1z} = -B_1 \cos\left(\frac{\pi(x-x_0)}{L}\right) \cos\theta_1 \exp\left(-\frac{\pi \sin\theta_1(y-y_0(t))}{L}\right). \tag{2}$$

Here $B_1 = 150$ G and $L = 20$ Mm. x_0 and $y_0(t)$ control the instantaneous location of the emerging flux, $x_0 = -30$ Mm, and we assume the center of the dipole is first located at $y_0(t=0) = y_c = -10$ Mm, then moves up with speed v_0. The emerging dipole is transported into the computational domain through the time-dependent electric field at the lower boundary, and the emergence stops after around 86 minutes. θ_1 is the angle between the emerging bipole and the $x-y$ plane. In this Letter, we set $\theta_1 = 0$, which means the emerging flux has a 60° angle to the background field.

The simulation employs a three-step Runge–Kutta time-integration method, with the "vanLeer" limiter and Harten–Lax–van Leer Riemann solver. We adopt the upwind constrained transport (CT) method to constrain the magnetic field divergence close to zero. We enforce symmetry of the density, total energy, y component of momentum, and B_y, while
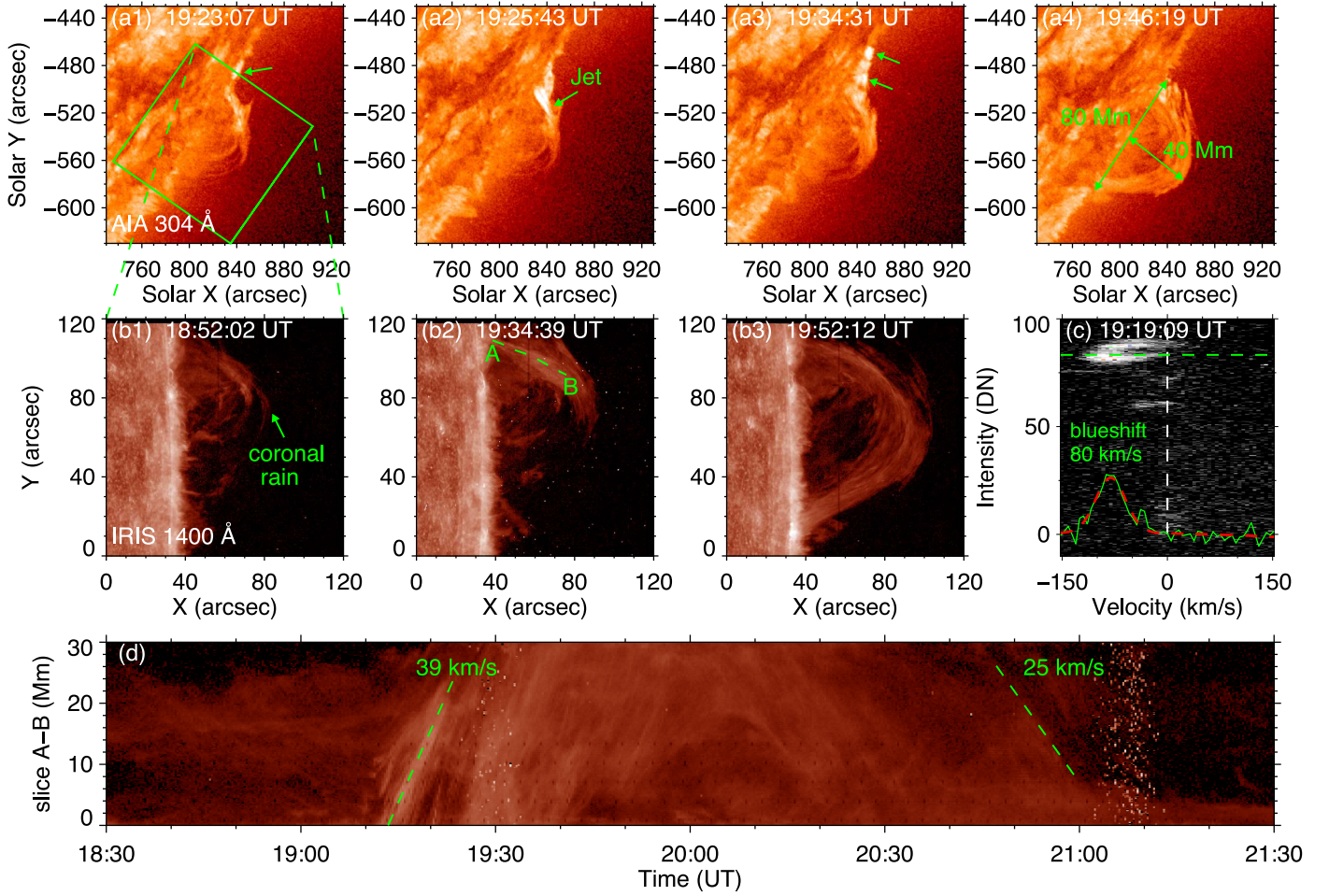

Figure 1. Observations of the eruptions on 2014 October 9. Panels (a1)–(a4) and panels (b1)–(b3) are AIA 304 Å images and IRIS 1400 Å images displaying the jet, respectively. The green rectangle in panel (a1) outlines the field of view (FOV) of panels (b1)–(b3). The green arrows in (a3) show the plasmoid-like structures. Panel (c) shows the Si IV 1403 Å spectra in the slit range of panel (b2) for Doppler velocities from -150 to 150 km s^{-1}. The solid green curve is the observed profile at the selected locations denoted by the dashed green line, and the dashed red curve is the corresponding single-Gaussian fitting. Panel (d) displays the temporal evolution of flows at the position of slice A–B (see panel (b2)). An animation accompanying this figure is available. The upper panel of the animation shows the AIA 304 Å observations from 18:50 UT to 20:58 UT on 2014 October 9; the cadence is 12 s and the spatial resolution is 0″6. The lower animation panel shows the IRIS 1400 Å observations at the same time, with a resolution of 0″166 pixel^{-1} and a cadence of 19 s.

(An animation of this figure is available.)

the x and z components of momentum, B_x, and B_z are forced to be antisymmetric at the left and right boundaries. For the bottom boundary, we set the velocity to zero, except for the emergence area where the velocity v_0 equals 2 km s^{-1}. The density and pressure are fixed as predetermined in the initial condition. At the top boundary, we use fixed zero velocity and extrapolate pressure and density according to the gravity stratification. We determine B_x and B_z with a zero-gradient extrapolation and derive B_y using the zero-divergence constraint at both the top and bottom boundaries. Our simulation includes gravity, field-aligned thermal conduction using the Runge–Kutta Legendre super-time-stepping scheme (Meyer et al. 2012, 2014), optically thin radiative losses handled with the exact integration method (Townsend 2009), randomized heating, and the transition region adaptive conduction method (Johnston & Bradshaw 2019; Zhou et al. 2021). This comprehensive set of physical mechanisms allows us to study the thermodynamic properties of the solar atmosphere more realistically.

4. Results

As in our previous paper (Li et al. 2022), after turning on the localized heating, thermal instability will occur, and condensations will form continuously in the loops, at first demonstrating a zigzag structure due to sympathetic runaway cooling on nested loops (Fang et al. 2013, 2015) as shown in the online animation associated with Figure 2. Starting from this coronal rain-filled arcade system at $t = 144.6$ minutes, we put an emerging flux at the left footpoint. As the emerging flux changes the pressure in the loops, the cool condensations move preferentially to the other side of the loop instead of splitting into small blobs and dropping to both footpoints as in the previous work (Fang et al. 2013, 2015; Li et al. 2022). Figure 2(a) shows the number density map and the magnetic field lines (in blue) at around 70 minutes after the emerging flux protrudes through the lower boundary. We can see that the emerging flux invades the corona with lower atmospheric plasma. After the emerging flux enters the corona, a current sheet is created on top of the emerging flux, and there is a dense loop located at the current sheet (see the Figure 2 animation especially at times $t = 209.0$–224.7 minutes), which is believed
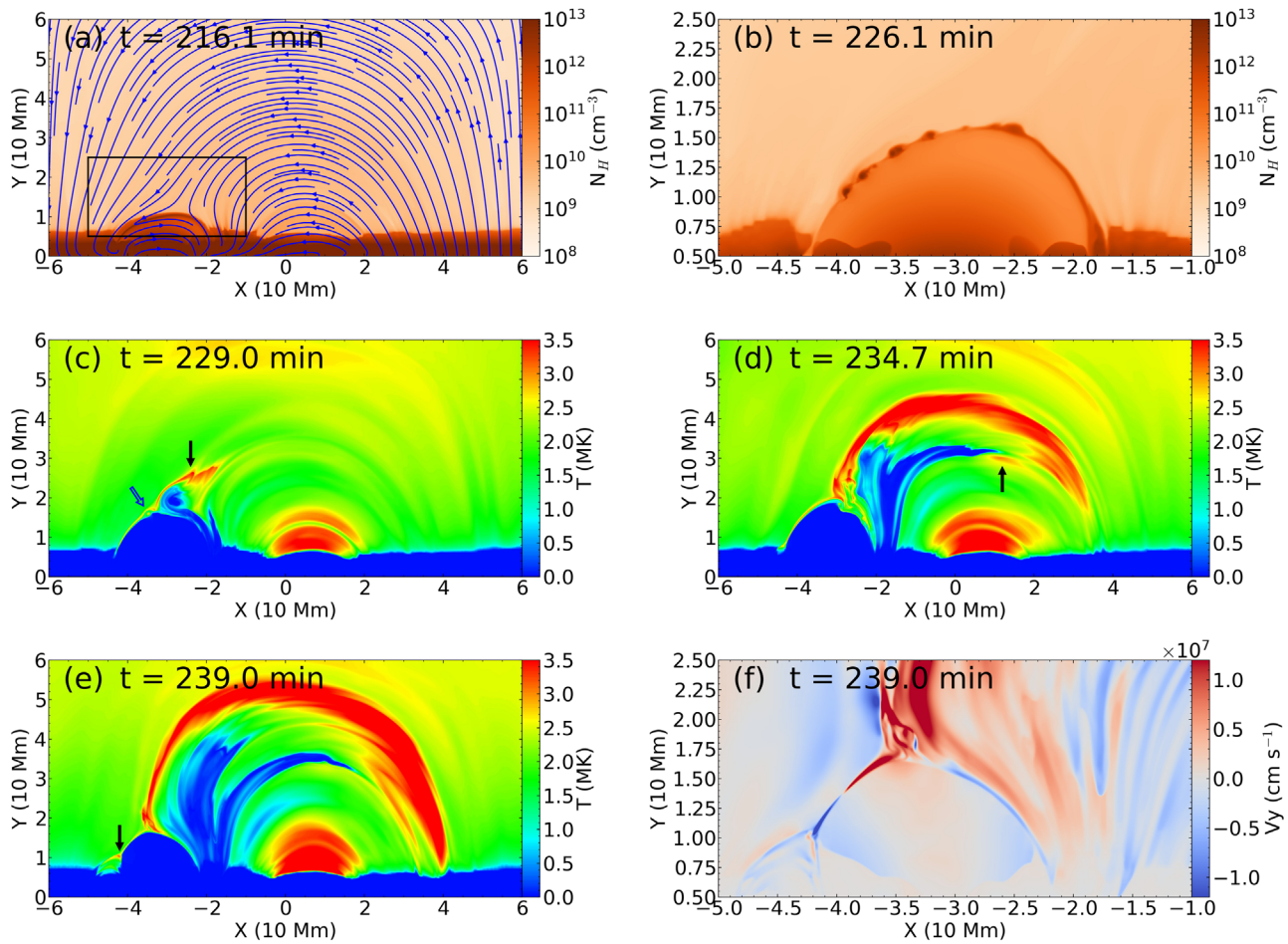
Figure 2. Simulations of flux emergence and the formation of eruptions. Panels (a) and (b) are the number density maps, and the FOV of panel (b) is denoted by the black rectangle in panel (a). The blue lines in panel (a) indicate the magnetic field lines. Panels (c)–(e) illustrate the temperature change of the domain during the flux emergence, and the arrows point to localized heating areas. Panel (f) is the vertical velocity map in the zoomed-in black rectangle area as shown in panels (a)–(b). An animation of this figure is available, showing the evolution of number density and temperature of our simulation from $t = 0$ minutes to $t = 300$ minutes. The time cadence of the animation is about 1.431 min.

(An animation of this figure is available.)

to be an arched filament (Zwaan 1985; Shibata et al. 1992). As the dipole is emerging upwards, multiple magnetic islands form in the current sheet due to the tearing instability, as displayed in Figure 2(b). Each island encloses dense and cool plasma originally in the emerging loop. The distance between each island is about 2.5 Mm. Soon after formation, the small islands merge into a large island, as shown in panel (c). Then, the resulting large island is ejected horizontally out of the current sheet. At the same time, the plasma near the current sheet is heated to a high temperature as denoted by the black arrow in panel (c). We also find hot plasmoids pointed out by the lower open blue arrows in panel (c) and in the online animation at $t = 227.6$ and 229.0 minutes. The temperature of the hot plasmoid is about 2.5 million Kelvin (MK). In panels (d) and (e), the ejection of the cool plasma forms a cold Hα surge with a temperature of 6000 K, and the nearby corresponding heating is manifested as a hot X-ray jet, whose temperature is more than 4 MK. In front of the Hα surge, we also find some heating (see the black arrow in panel (d)), which may be caused by shock waves (Forbes & Priest 1983; Pontin & Priest 2022). The arrows in panel (e) and the online animation between $t = 236.2$–240.4 minutes denote the heating near the transition region (TR) which could be recognized as a flare or bright point

in observations. Panel (f) shows the vertical velocity, and there are clear bidirectional flows at the upper and lower edges of the current sheet, which is one of the typical manifestations of magnetic reconnection (Innes et al. 1997; Li et al. 2018). These outflows have velocities around 400 km s^{-1} (of order the local Alfvén speed, as expected from reconnection theory).

The number density maps in Figure 3 display the dynamics of the jet. We can clearly see that the jet shows transverse oscillations, which have been termed as whiplike motions (Canfield et al. 1996; Morton et al. 2012; Chandrashekhar et al. 2014). As mentioned in the last paragraph, the emerging flux, which carries the cool plasma from the chromosphere, expands upward and reconnects with the preexisting coronal loops, forming magnetic islands and bidirectional flows. As the magnetic tension of disconnected field lines drives the plasmoid to move outwards and as it experiences the slingshot effect, the magnetic field line gets stretched and bent due to the heavy plasma load, as shown in Figure 3(a1). As the jet shows a whiplike motion, the plasma inside the jet has a motion perpendicular to the magnetic field lines, and the shape of these field lines changes accordingly, as shown by the blue curves in panels (a2) and (a3). To investigate the motion of the jet more clearly, we make two slices along the positions denoted by the
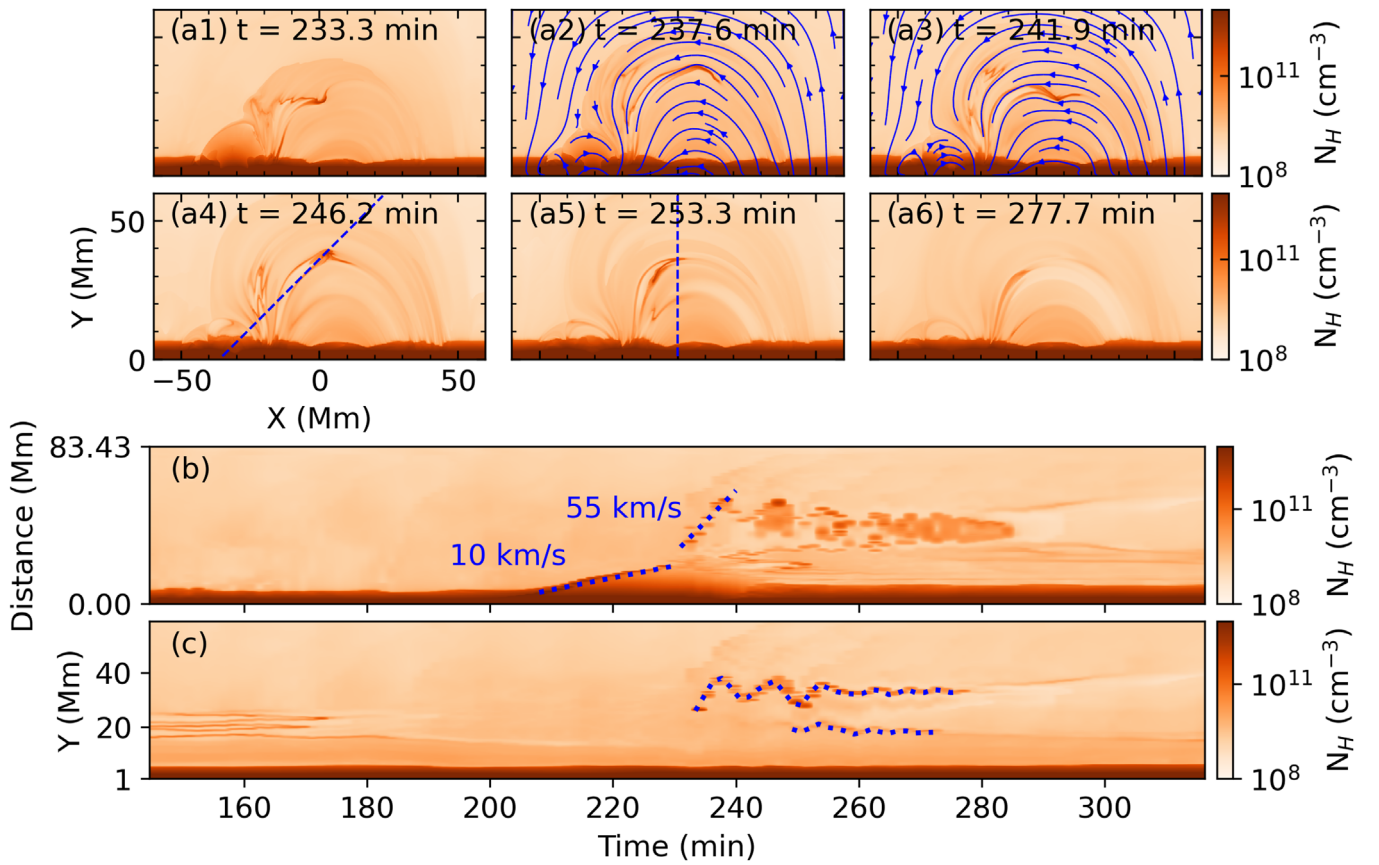
Figure 3. Number density maps showing the whiplike motion of the jet. Panel (b) is the time–distance plot of the number density along the position indicated by the dashed blue line in panel (a4). Panel (c) shows the evolution of the number density along the *y*-direction as denoted by the dashed blue line in panel (a5). The dotted blue curves display the oscillations of the jet and the movement of condensations in the lower loops.
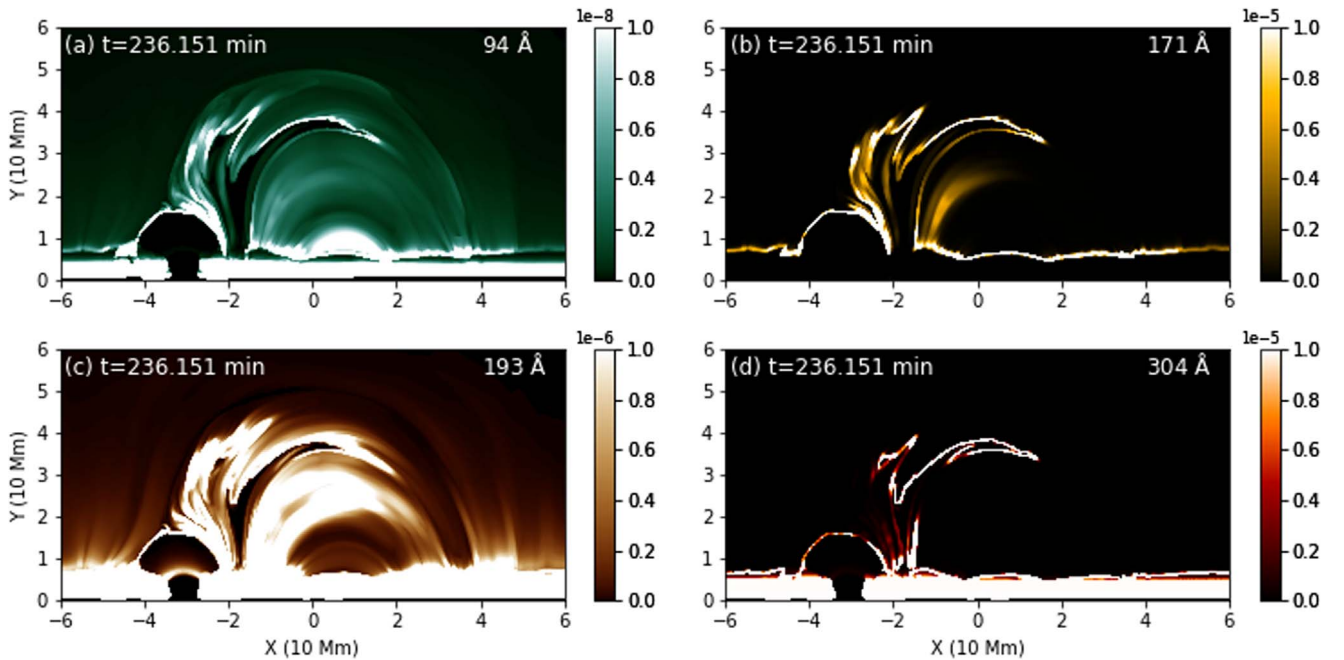
Figure 4. AIA 94, 171, 193, and 304 Å synthetic images showing the eruptions at the selected time.

dashed lines in panels (a4) and (a5), and the evolution of the number density along these two positions is shown in Figures 3(b) and 3(c), respectively. From panel (b), we can see that the emerging loop rises with a velocity of 10 km s^{-1}, in

agreement with previous simulations and observations (Chou & Zirin 1988; Shibata et al. 1989; González Manrique et al. 2018; Tiwari et al. 2019). After the reconnection, the cool materials are ejected upwards with a velocity of ~55 km s^{-1}, which is
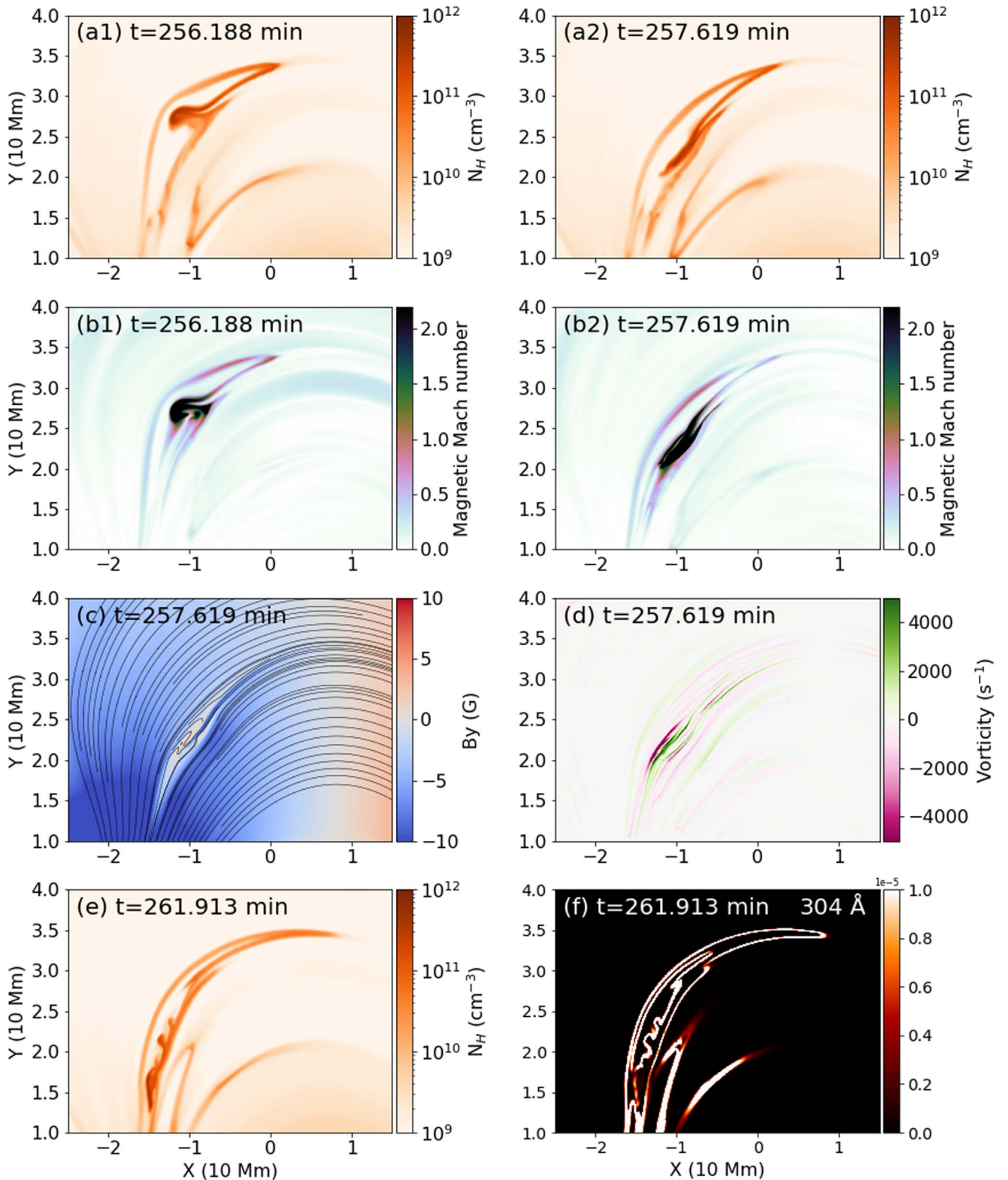
Figure 5. The occurrence of KHI. Panels (a1)–(a2) and panels (b1)–(b2) are the number density and Mach number maps at $t = 256.188$ and $t = 257.629$ minutes. Panel (c) and panel (d) show the distributions of the magnetic field in the y-direction and the vorticity at $t = 257.619$ minutes, respectively. The number density map in panel (e) and the synthetic AIA 304 Å image in panel (f) display the vortex-like structures caused by the KHI at $t = 261.913$ minutes.

comparable to the observed velocity of the jet. In panel (c), the upper dotted blue curve shows the whiplike motion of the jet, which in this time–distance view just appears as a damped transverse oscillation. The period of this oscillation is about 8 minutes. Not only does the magnetic field with the jet material

have whiplike motions, but the whole loop system is oscillating vertically. As a result, condensations inside the underlying loops also displays forced oscillation, as shown by the lower dotted curve in panel (c).

Using the technique described in Xia et al. (2014), we also obtain EUV synthetic images to compare the result with the AIA observations. Figure 4 demonstrates the morphology of the jet in 94, 171, 193, and 304 Å wave channels at $t = 236.151$ minutes, which corresponds to plasma with temperatures of around 6.3, 0.8, 1.5, and 0.08 MK, respectively. In the hot 94 Å image in panel (a), the hot X-ray jet could be observed as a bright feature, and the cool jet is dark. The cool jet also looks dark inside and bright at the boundary in the 171 and 193 Å channels. The positions near the reconnection area and the jet front are especially brighter in the 193 Å channels, which is due to the heating caused by the reconnection and the shock. In the cool 304 Å channel, the jet has a dark core and bright edges, which is an artifact of our 2.5D assumption since the boundary area of the jet has a TR temperature, which responds to the 304 Å channels. We speculate that in a 3D simulation, the whole jet will look bright in 304 Å channels.

As mentioned in Figure 3, the movement of the plasmoid will change the shape of the local magnetic field lines, and we find that at scales accessible to current resolutions, this may trigger the Kelvin–Helmholtz instability (KHI; e.g., Keppens et al. 1999; Tian & Chen 2016; Ni et al. 2017). The KHI happens when two flows with strong velocity shears move along each other. In magnetized plasma, the occurrence of the KHI requires the total velocity difference to be more than a threshold, which is basically 2 times the Alfvén velocity since a parallel magnetic field component can suppress KHI growth. As shown in Figures 5(a1) and (a2), a heavy plasma blob drops from the top of the coronal loops. As the blob falls down, the magnetic field line becomes curved and stretched so the weakened parallel magnetic fields can no longer suppress the KHI. This is shown by the Mach number maps in panels (b1) and (b2), where the Mach number at the interface is higher than 2, the threshold for the KHI. The deformed magnetic field is shown by the black curves in panel (c). This falling plasma blob has a velocity difference with the ambient plasma, as seen by the vorticity map in panel (d). As the KHI happens, the boundary of the falling jet blobs display vortex-like structures shown in panel (e). There have been some observational works showing vortex-like structures at the edge of the jet (Li et al. 2018, 2019), and we present a synthetic AIA 304 Å image in panel (f) to compare with observations. The size of the vortex-like structures is approximately 1.5 Mm, which is consistent with the observations.

5. Conclusion and Discussions

In this Letter, we report an event observed by SDO and IRIS where flux emergence at the northern end of a closed coronal loop system causes the eruption of plasma, forming a jet with an apparent velocity of 39 km s^{-1} and a Doppler blueshift of 80 km s^{-1}. Adopting our open-source code MPI-AMRVAC, we perform a 2.5D MHD simulation which produces eruptions resulting from the flux emergence with a magnetic flux intensity of 150 G at the left footpoint of the loop. At first, the loops have coronal rain material inside them, and this coronal rain all moves to the other (right) side of the loops since the emergence influences the pressure gradient inside the loops. Reconnection between the emerging flux and the preexisting loops forms a dense-plasma-loaded current sheet at the interface, and then magnetic islands and bidirectional flow appear. The magnetic islands coalesce into one blob and

then is ejected outwards, forming a cool jet that has a similar length, height, and velocity as the observations. The nearby plasma is heated to more than 4 MK, manifested as a hot jet. The hot jet could be observed as a bright feature in the synthetic 94 Å images, and the cool jet is dark in the 94, 171, and 193 Å channels. The jet exhibits distinct whiplike motions and induces similar oscillations in the condensations in the loops beneath it. The movement of the jet material changes the local magnetic field configuration, which allows the occurrence of the KHI, and as a result, vortex-like structures form at the edge of the jet.

Combined computational and observational efforts are needed to understand the interaction between flux emergence and dynamic atmospheric activities (Fan & Gibson 2004; Cheung & Isobe 2014; Archontis & Syntelis 2019). We have successfully reproduced a lot of features reported in previous observations and simulations, such as magnetic islands, the simultaneous existence of hot and cool jets, whiplike motions, and vorticity structures due to KHI. Compared to the observed event, the jet we get has nearly the same properties (e.g., length, height, and velocities) as the observations. Our results confirm that magnetic reconnection between the emerging flux and overlying loops causes a series of coronal eruptions. There are a lot of parameters that could influence the trigger of the eruptions, such as the emerging magnetic flux strength (B_1) and the relative angle (related to θ_1 in our setup) between the emerging flux and the arcade (Leake et al. 2022). In follow-up work, we will present a detailed parameter survey to determine which parameters play the most prominent roles.

Our simulation reveals that the influence of the moving multithermal plasma jet on the magnetic field can promote the KHI happening. Using a 2D MHD simulation, Ni et al. (2017) found that when the jet is ejected upwards, KHI could contribute to the formation of blob structures near the current sheet in a high β case ($\sim$0.15–1.5). Li et al. (2018, 2019) suggested that KHI may be responsible for the vortex-like structures formed both during the upstream and downstream of the jets in the observations. In our simulation, the plasma β around the place where the KHI happens is around 0.45. The movement of the jet materials could bend the magnetic field, making the local Mach number exceed the threshold of the KHI, resulting in vortex-like structures at the boundary of the jet. The scale of the vortex-like structures is similar to the observations. In the simulation, the high Mach number regions only exist for several minutes and break down soon after, leading to the suppression of the KHI, and then the vortex-like structures disappear. This explains why only a few KHI cases have been observed in jets so far, and we expect that more KHI cases could be found in higher resolution observations. Also, it is important to revisit this setup to achieve a more comprehensive understanding of the system's behavior in full 3D settings.

ORCID iDs

Xiaohong Li ● https://orcid.org/0000-0001-8164-5633
Rony Keppens ● https://orcid.org/0000-0003-3544-2733
Yuhao Zhou ● https://orcid.org/0000-0002-4391-393X

References

Archontis, V., Moreno-Insertis, F., Galsgaard, K., Hood, A., & O'Shea, E. 2004, A&A, 426, 1047
Archontis, V., & Syntelis, P. 2019, RSPTA, 377, 20180387
Caligari, P., Moreno-Insertis, F., & Schussler, M. 1995, ApJ, 441, 886
Canfield, R. C., Reardon, K. P., Leka, K. D., et al. 1996, ApJ, 464, 1016
Chandrashekhar, K., Bemporad, A., Banerjee, D., Gupta, G. R., & Teriaca, L. 2014, A&A, 561, A104
Chen, F., Rempel, M., & Fan, Y. 2017, ApJ, 846, 149
Chen, P. F. 2011, LRSP, 8, 1
Chen, P. F., & Shibata, K. 2000, ApJ, 545, 524
Cheung, M. C. M., & Isobe, H. 2014, LRSP, 11, 3
Cheung, M. C. M., Rempel, M., Chintzoglou, G., et al. 2019, NatAs, 3, 160
Cheung, M. C. M., Rempel, M., Title, A. M., & Schüssler, M. 2010, ApJ, 720, 233
Chou, D.-Y., & Zirin, H. 1988, ApJ, 333, 420
De Pontieu, B., Title, A. M., Lemen, J. R., et al. 2014, SoPh, 289, 2733
Fan, Y. 2001, ApJL, 554, L111
Fan, Y. 2021, LRSP, 18, 5
Fan, Y., & Gibson, S. E. 2004, ApJ, 609, 1123
Fang, X., Xia, C., & Keppens, R. 2013, ApJL, 771, L29
Fang, X., Xia, C., Keppens, R., & Van Doorsselaere, T. 2015, ApJ, 807, 142
Feynman, J., & Martin, S. F. 1995, JGR, 100, 3355
Forbes, T. G., & Priest, E. R. 1983, SoPh, 84, 169
González Manrique, S. J., Kuckein, C., Collados, M., et al. 2018, A&A, 617, A55
Guglielmino, S. L., Bellot Rubio, L. R., Zuccarello, F., et al. 2010, ApJ, 724, 1083
Guglielmino, S. L., Zuccarello, F., Young, P. R., Murabito, M., & Romano, P. 2018, ApJ, 856, 127
Hansteen, V., Ortiz, A., Archontis, V., et al. 2019, A&A, 626, A33
Heyvaerts, J., Priest, E. R., & Rust, D. M. 1977, ApJ, 216, 123
Innes, D. E., Inhester, B., Axford, W. I., & Wilhelm, K. 1997, Natur, 386, 811
Jiang, C., Wu, S. T., Feng, X., & Hu, Q. 2016, NatCo, 7, 11522
Johnston, C. D., & Bradshaw, S. J. 2019, ApJL, 873, L22
Keppens, R., Meliani, Z., van Marle, A. J., et al. 2012, JCoPh, 231, 718
Keppens, R., Teunissen, J., Xia, C., & Porth, O. 2021, CMwA, 81, 316
Keppens, R., Tóth, G., Westermann, R. H. J., & Goedbloed, J. P. 1999, JPlPh, 61, 1

Kliem, B., & Török, T. 2006, PhRvL, 96, 255002
Leake, J. E., Linton, M. G., & Antiochos, S. K. 2014, ApJ, 787, 46
Leake, J. E., Linton, M. G., & Antiochos, S. K. 2022, ApJ, 934, 10
Leake, J. E., Linton, M. G., & Török, T. 2013, ApJ, 778, 99
Lemen, J. R., Title, A. M., Akin, D. J., et al. 2012, SoPh, 275, 17
Li, X., Keppens, R., & Zhou, Y. 2022, ApJ, 926, 216
Li, X., Zhang, J., Yang, S., & Hou, Y. 2019, ApJ, 875, 52
Li, X., Zhang, J., Yang, S., Hou, Y., & Erdélyi, R. 2018, NatSR, 8, 8136
Lionello, R., Török, T., Titov, V. S., et al. 2016, ApJL, 831, L2
Manchester, W. I., Gombosi, T., DeZeeuw, D., & Fan, Y. 2004, ApJ, 610, 588
Meyer, C. D., Balsara, D. S., & Aslam, T. D. 2012, MNRAS, 422, 2102
Meyer, C. D., Balsara, D. S., & Aslam, T. D. 2014, JCoPh, 257, 594
Miyagoshi, T., & Yokoyama, T. 2004, ApJ, 614, 1042
Moreno-Insertis, F., Galsgaard, K., & Ugarte-Urra, I. 2008, ApJL, 673, L211
Moreno-Insertis, F., Martinez-Sykora, J., Hansteen, V. H., & Muñoz, D. 2018, ApJL, 859, L26
Morton, R. J., Srivastava, A. K., & Erdélyi, R. 2012, A&A, 542, A70
Ni, L., Zhang, Q.-M., Murphy, N. A., & Lin, J. 2017, ApJ, 841, 27
Nóbrega-Siverio, D., & Moreno-Insertis, F. 2022, ApJL, 935, L21
Nóbrega-Siverio, D., Moreno-Insertis, F., & Martínez-Sykora, J. 2016, ApJ, 822, 18
Pesnell, W. D., Thompson, B. J., & Chamberlin, P. C. 2012, SoPh, 275, 3
Pontin, D. I., & Priest, E. R. 2022, LRSP, 19, 1
Porth, O., Xia, C., Hendrix, T., Moschou, S. P., & Keppens, R. 2014, ApJS, 214, 4
Schmieder, B., Archontis, V., & Pariat, E. 2014, SSRv, 186, 227
Schrijver, C. J. 2009, AdSpR, 43, 739
Shen, J., Xu, Z., Li, J., & Ji, H. 2022, ApJ, 925, 46
Shibata, K., Nozawa, S., & Matsumoto, R. 1992, PASJ, 44, 265
Shibata, K., Tajima, T., Steinolfson, R. S., & Matsumoto, R. 1989, ApJ, 345, 584
Shimojo, M., Shibata, K., Yokoyama, T., & Hori, K. 2001, ApJ, 550, 1051
Tian, C., & Chen, Y. 2016, ApJ, 824, 60
Tiwari, S. K., Panesar, N. K., Moore, R. L., et al. 2019, ApJ, 887, 56
Toriumi, S. 2022, AdSpR, 70, 1549
Toriumi, S., & Wang, H. 2019, LRSP, 16, 3
Török, T., Lionello, R., Titov, V. S., et al. 2016, in ASP Conf. Ser. 504, Coimbra Solar Physics Meeting: Ground-based Solar Observations in the Space Instrumentation Era, ed. I. Dorotovic, C. E. Fischer, & M. Temmer (San Francisco, CA: ASP), 185
Townsend, R. H. D. 2009, ApJS, 181, 391
Turk, M. J., Smith, B. D., Oishi, J. S., et al. 2011, ApJS, 192, 9
van Driel-Gesztelyi, L., & Green, L. M. 2015, LRSP, 12, 1
Wang, J., Liu, C., Cao, W., & Wang, H. 2020, ApJ, 900, 84
Xia, C., Keppens, R., Antolin, P., & Porth, O. 2014, ApJL, 792, L38
Xia, C., Teunissen, J., El Mellah, I., Chané, E., & Keppens, R. 2018, ApJS, 234, 30
Yokoyama, T., & Shibata, K. 1995, Natur, 375, 42
Yokoyama, T., & Shibata, K. 1996, PASJ, 48, 353
Zhou, Y. H., Chen, P. F., Hong, J., & Fang, C. 2020, NatAs, 4, 994
Zhou, Y.-H., Ruan, W.-Z., Xia, C., & Keppens, R. 2021, A&A, 648, A29
Zwaan, C. 1985, SoPh, 100, 397
Zwaan, C. 1987, ARA&A, 25, 83